JOURNAL OF THE AMERICAN HELICOPTER SOCIETY **57**, 042006 (2012)

Prediction of Brownout Inception Beneath a Full-Scale Helicopter Downwash


Gregory Jasion
Ph.D. student

John Shrimpton*
Reader

Aerodynamics and Flight Mechanics Research Group
University of Southampton, Southampton, UK

Dust entrained by low flying helicopters leads to the degraded visual environment, brownout. Particle inception is a critical stage in the development of the dust cloud. Here, near-wall Lagrangian particle forces are considered through analyzing an approximate time-averaged full-scale rotor flow. This simplified flow does not attempt to predict brownout, instead it provides scales and velocity data in the near-wall region, compares the role of particle-fluid forces, and provides a foundation for Lagrangian entrainment models. The analysis shows that three characteristic particle sizes are exposed to different physics in different boundary layer zones, a function of the distance from the helicopter. Drag is the dominant aerodynamic force, cohesion is large for small particles, but wall-bounded lift is sufficient to entrain medium-sized particles. A complementary analytical prediction of tip vortices found that both large-scale inviscid features and small-scale viscous features of the boundary layer are significant.

Nomenclature

Symbols

A	area
a	asperity moment arm
a_1	Squire parameter
C	coefficient
D	diameter
F	force
Fr	Froude number
f	correction factor
g	gravity
k	turbulent kinetic energy
m	mass
Re	Reynolds number
r	radial coordinate
r_c	vortex core radius
r_p	particle radius
r_v	vortex radial position
r_{c0}	initial vortex radius
$\bar{r}$	nondimensional radial position, r_v/r_c
St	Stokes number
T	thrust
u	velocity
y	vertical coordinate
α	Lamb constant
Γ_v	tip vortex circulation
δ	vortex dissipation constant
ϵ	turbulent dissipation rate
ζ	wake age, rad
μ	dynamic viscosity
ν	kinematic viscosity
ρ	density
τ	timescale
Ω	blade angular velocity, rads^{-1}

Subscripts

disk	rotor disk
f	fluid
p	particle
wall	wall
0	reference
τ	shear based
∞	downstream

Force Subscripts

B	Basset
D	drag
Fr	friction
G	gravity
H	horizontal
L	lift

*Corresponding author: email: john.shrimpton@soton.ac.uk.
Manuscript received October 2011; accepted August 2012.

DOI: 10.4050/JAHS.57.042006

M	Magnus
P	pull-off, cohesion
S	Saffman
ϕ	ambiguous force term

Superscripts

$+$	nondimensional term
$*$	nondimensional variable in the force analysis

Introduction

Brownout is the name given to the occurrence of thick clouds of dust generated by helicopters during landing and takeoff in dusty conditions. When this happens, the visibility of the pilot is degraded so much that only brown dust can be seen and is therefore likened to redout and blackout effects associated with high *g*-force maneuvers. Whiteout is the name for the snow equivalent of brownout. Pilots attempting to land rotorcraft in this degraded visual environment take a large risk; without visual cues, the craft is likely to drift which could result in rollover and the loss of the aircraft and crew.

The main driver for studying brownout is the recent increase of military operations in desert theaters. In 2005, Lt. Col. Steve Colby of the United States Air Force reported in Ref. 1 that brownout had claimed more helicopters than any other threat. It is claimed in Ref. 2 that the phenomenon cost the U.S. military $100 million in 2006. The condition has a variety of impacts on operations including formation flying and troop insertion and generally poses an increased mission risk. Brownout also has an impact on civil operations; several brownout incidents have been reported over the last few years (Ref. 3).

The underlying process by which brownout occurs can be summarized as follows:

1) The air flow from the helicopter downwash spreads out across the ground surface.

2) The particles on the surface experience aerodynamic forces from the near ground flow.

3) The aerodynamic force on each particle must first overcome the cohesive forces and gravity that keeps the particle stationary.

4) Several hypotheses are proposed to lift the particle into the flow, either by an unsteady ejection event in the flow (Ref. 4), by rolling and bouncing the particle off of an asperity on the surface (Ref. 5), or through resonance (Ref. 6).

5) The liberated particle is now acted upon by the aerodynamic forces and gravity. For larger particles, saltation will probably result; that is, the particle will fall back down to the surface and collide with other particles on the ground.

6) This collision can liberate further particles via two means: The first is ballistic, the direct transfer of kinetic energy through collision, and the second is the wake of the incident particle entraining finer particles. The indirect effect of displacing the larger particles is that this may expose smaller particles that were previously hidden from the flow.

7) If the particle described in stage 5 is small, it will follow the flow and can be considered entrained. The particle will still be influenced by gravity and so will drop out of the cloud if the aerodynamic forces are not strong enough to keep it entrained.

The process enumerated above highlights the large range of scales involved. In this problem, there are flow features defined by rotor diameters of the order of several meters and there are particles of the order of micrometers reacting to the flow. Similarly, the modeling of the mechanics of saltation and brownout inception requires the tracking of many thousands of interacting particles. Combining knowledge from the different length and timescales of the problem is one of the primary challenges of this research area.

Brownout Entrainment Studies

One of the earliest studies was by Rodgers (Ref. 7) in a full-scale experimental study on the dust cloud generated by rotor downwash. Dust samplers were mounted on the fuselage to determine the size distribution of airborne particles for different heights of hover. The result suggests that the stronger flow, when the helicopter is closer to the ground, is capable of entraining large and small particles alike, but a weaker downwash can only entrain the smaller particles. Gillies et al. carried out a recent full-scale experimental study measuring dust emission from low-level rotorcraft flight detailed in Ref. 8. The Sandblaster project (Ref. 9) gathered data of rotorcraft dust emission including particle size and concentrations. They conclude that larger airframes, with a higher disk loading, generate the densest dust clouds and are also capable of entraining the largest particles; concentrations of fine particles are similar for all airframes.

Lee and Leishman (Ref. 10) used digital particle image velocimetry (PIV) to look at the blade vortex ground interaction and the near ground velocity profile for a model rotor in ground effect. They conclude that the flow becomes an unsteady radially expanding wall jet and that the vortex filaments shed from the rotors normally diffuse naturally when the rotor is high enough from the ground. However, when the rotor is close to the ground the filaments spread out across the surface, causing them to spin up before turbulence in the wall jet quickly shears the vortices and accelerates their diffusion.

Johnson et al. (Ref. 11) conducted a multiphase PIV study to quantify the entrainment mechanisms for an in ground effect (IGE) rotor flow. The study captured vortex ground interactions with fascinating results involving the flow field around the vortices themselves, stagnation bubbles, and particle–vortex trapping. Johnson et al. question the validity of the threshold velocity dust models used in most brownout models comparing the upwash sources. The vertical flow in the turbulent boundary layer, for which the threshold velocity model was designed, is a result of only the turbulence where as an IGE rotor flow contains significant vertical flow from vortex events.

Haehnel and Dade (Ref. 12) investigated brownout by experiment, using a jet impinging on a bed of loose sand. The rig used a high-speed jet positioned directly above a large bed of sand or glass beads, the erosion of the bed was recorded. Haehnel and Dade concluded that it was possible to model entrainment rates if models were based on the Reynolds stresses, i.e., the turbulent fluctuations, but not on average velocity properties. The difference between this experiment and rotor-based entrainment is that rotor flow has strong vortex–ground interaction as shown by the results of Lee and Leishman. Haehnel and Dade include the fluctuation flow properties, but these are still Reynolds averaged and do not include the peak stresses from vortex events.

McAlpine et al. (Ref. 13) performed a steady-state full-scale numerical model attempting to characterize dust emissions; they used a steady computational fluid dynamics (CFD) simulation to find upwash regions associated with dust entrainment. The results are reasonable, but they do not go so far as to predict the shape of the dust cloud.

In recent years, several numerical models describing the complete brownout process have been presented. Among the work present are models developed by Wachspress et al. of Continuum Dynamics in Ref. 14, Philips and Brown of Glasgow University in Ref. 15, D'Andrea of Augusta Westland (Ref. 16), and Syal et al. of the University of Maryland (Ref. 17). The aim of these developments is to create a complete brownout simulation package by incorporating CFD with a particle motion method and an entrainment model. A short account of the entrainment models used in the simulations of Wachspress and Philips is given here.

The simulation developed by Wachspress et al. incorporates a Lagrangian tracking model with a vortex transport CFD model. The objective was to develop a deterministic real-time brownout simulation. The flow is solved using a free-vortex model based on potential flow; it is essentially inviscid although the dissipation of vortex strength due to the ground boundary layer is accounted for using an analytic model. They use an entrainment criteria based on a threshold friction velocity; the velocity at a reference height is supplied by the CFD model, and this is then used to find the shear stress on the ground via a logarithmic boundary layer profile. If the friction velocity generated by the flow field exceeds the threshold, particles are entrained. Once entrained, the particles are carried through the flow by the drag force based on the relative velocity. This model is empirical and correlates qualitatively with pilot experience and photographic evidence. The model makes predictions of the dust concentrations along the fuselage of a tandem helicopter; the results are a good match with experiments by Rodgers in Ref. 7.

The experiments by Haehnel and Dade show that results correlate best with the peak velocity events rather than averaged velocities. Wachspress' model is driven by an unsteady CFD code such that the velocity values put into the model are instantaneous. The entrainment flux expression is a macroscopic expression based on observation; there is no appreciation of how the flow interacts with the surface particles and since the expression was defined for aeolian transport the idiosyncrasies of the vortical rotor downwash are not appreciated.

The Philips and Brown model (Ref. 15) is Eulerian. The particles are modeled as a continuum in the flow. The entrainment model is a source term in a particle transport equation. Philips and Brown used a similar threshold expression to Bagnold and used wind tunnel data from Lu and Shao (Ref. 18) to find values of model constants. The model is simplified to only use one roughness scale, one particle diameter, and therefore has a uniform threshold velocity. A horizontal flux model from White (Ref. 19) is used to determine the number of particles that are saltated. A fraction of these are fully entrained, that fraction is determined by the clay content of the soil base.

The entrainment model is handled in much the same way as a wall function in a CFD code, but this is developed based on the steady parallel flows from aeolian research such as Bagnold in Ref. 20. The flow features that make the rotor flow significant are ignored in the entrainment model, and all saltation is assumed to happen in this near-wall region.

The basic aeolian saltation models do not always capture the unsteady effects or the effect of near-wall vortices. Unsteady aeolian dust entrainment is investigated by Bauer et al., Butterfield, and Spies and McEwan in Refs. 21, 22, 23, respectively. In each study, conditional averaging and event detection are used to consider sweep and ejection events but their results were inconclusive. Sterk et al. (Ref. 24) found that the fluctuation events, sweeps, and ejections contribute positively and negatively to shear stress but only positively to saltation and streamwise velocity; they conclude that the driving variables are wind speed and fluctuations not shear stress as is commonly considered in the Bagnold model.

Cao uses the average bursting frequency for parallel, uniform, and steady turbulent flows in Ref. 4. A bursting period relationship is related to the friction velocity $T_B = \nu T_B^+/u_*^2$, where T_B is the bursting period and $T_B^+ = 100$ is the nondimensional bursting period found from the literature. The concept of a bursting period could be used, perhaps drawing parallels to the frequency of rotor tip vortex impacts with the ground or the turnover time of a vortex structure. Aerosols from reactor explosions were studied by Ardey and Mayinger in Ref. 25; entrainment following a sudden pressure wave is greater than the equivalent steady flow case, which supports the importance of vortical events in rotor wash entrainment.

Marchioli et al. (Ref. 26) looked at the power of near-wall turbulent events to eject particles from the surface; the power analysis focused on the boundary layer of a wavy wall. The vortical structures seen by Marchioli reach into the shear layer, and strong sweep and ejection events occur. The vortices are identified as the principle driver for particle resuspension with Stokes number being the controlling parameter. The helicopter flow may not have the same structure, but it features unsteady vortical structures that could cause the particles to be entrained in like manner.

Marchioli and Cao both produce entrainment functions with agreeable results in the parallel flow case, but there appears to be an absence of understanding between the single particle leaving a surface and the surface mass flux approach. A function that is capable of expressing the entrainment from a finite event while maintaining the capacity to integrate with a full brownout model is a likely solution for an entrainment model in such an inhomogeneous flow as that of an IGE rotor wash.

This paper aims to highlight the key forces that act on the particles on the ground and contribute to a multiscale entrainment model suitable for simulating the rotorcraft phenomena of brownout. This paper presents a nondimensional analysis of particle–fluid forces to assess the significance of each contributing force and then compares those findings with the forces a particle experiences in a time-averaged helicopter downwash flow field calibrated against results of Rodgers (Ref. 7). The forces are calculated on three different particle sizes in the near-wall region to discover how each particle size is stimulated by the flow. The blade tip vortex contribution is assessed analytically, and the impact they have on the mean flow results is discussed. We aim to discover which of the model assumptions described above are transferable to a Lagrangian-based entrainment model by comparing them with the results presented in this paper.

The Helicopter Flow Field

The flow field analysis has been split into two parts: the viscous mean flow with turbulent fluctuations and an inviscid tip vortex analysis. The bulk of the analysis in this study is carried out using the mean flow results. The tip vortex analysis uses the mean flow field to estimate the vortex path, lift from the rotor to estimate circulation, and an analytical method to calculate the induced velocity profile around the vortex.

Reynolds-averaged Navier–Stokes flow field

A full-scale experiment of a helicopter hovering above the ground, performed by Rodgers in Ref. 7, was simulated with Fluent, version 12.0.16, using the Reynolds-averaged Navier–Stokes (RANS) equations. The horizontal velocities of Rodgers up to 0.1 m from the ground at different radial distances from the rotor hub are reported in Fig. 1. The simple steady two-dimensional axisymmetric domain consisted of a rotor of diameter $D_{\text{disk}} = 11.32$ m hovering at height $z/D_{\text{disk}} = 0.34$ from the ground.

The axis cut vertically through the rotor hub and was the west boundary. The south boundary was the ground and had a nonslip wall condition. The north and east boundaries were modeled as constant gauge pressure boundaries and were positioned $2.5D_{\text{disk}}$ and $4.5D_{\text{disk}}$ from the ground and axis boundary, respectively. The rotor was modeled as momentum source injected into cells at the rotor position, a region 0.1 m thick. The mesh contained 400 × 200 nodes, concentrated near the axis and the wall with the first node at $y^+ \simeq 1$ to capture the viscous sublayer. In addition, we ensured that the first node resolved the flow to the scale of the particles. A realizable $k - \epsilon$ turbulence model (Ref. 27) was used because of its favorable performance in axisymmetric jets, and a two layer nonequilibrium wall model (Ref. 28) was chosen because of the

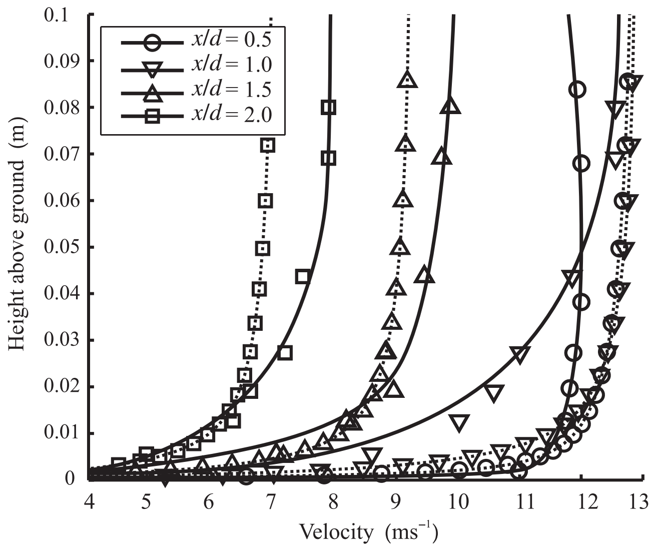

Fig. 1. U.S. Army Engineer Waterways Experimental Station (USWES) experimental data from Ref. 7 (solid line) compared with the RANS results (dotted line).

strong pressure gradients. In essence, we have chosen to resolve the full range of length scales at the expense of unsteady flow structures.

To find the air velocity through the rotor a one-dimensional momentum balance was conducted for the hovering helicopter IGE. Assuming the flow to be incompressible, inviscid and steady then a simple momentum balance from Ref. 29 provides Eq. (1):

$$T = \dot{m}(u_\infty - u_0) \tag{1}$$

where T is the thrust the disk exerts on the fluid, $\dot{m}$ is the mass flux through the disk, u_∞ is the velocity far downstream, and u_0 is the velocity far upstream. A control volume is applied around the disk, and the volume of air above the rotor to where the velocity $u_0 = 0$ and below the disk where the velocity is u_∞. Applying the momentum and energy equations yields Eq. (2):

$$T u_{\text{disk}} = \frac{1}{2}\dot{m}u_\infty^2 \tag{2}$$

with $\dot{m}$ given in Eq. (3):

$$\dot{m} = \rho u_{\text{disk}} A_{\text{disk}} \tag{3}$$

where u_{disk} is the velocity through disk and A_{disk} is the area of the disk. The Bell H13 helicopter empty mass is 858 kg and has a maximum take off mass of 1350 kg, with pilot and fuel the total craft is estimated to weigh 8.8 kN. The blade diameter is $D_{\text{disk}} = 11.32$ m, which gives a disk area of 100 m^2. These parameters result in an induced disk velocity of $u_{\text{disk}} = -6$ ms^{-1} and a mass flux of $\dot{m} = 725$ kgs^{-1}.

Flow field results

The RANS flow field results obtained were accurate to within 20% of the full-scale experimental results of Rodgers, but the general trend and magnitudes were consistent for the scaling analysis performed in this work. Figure 1 shows the RANS results directly compared with Rodgers. In addition, the radial flow field compares well with the small-scale experimental results of Lee et al. (Ref.10), scaled with the induced velocity at the disk.

It is commonly accepted that the peak velocity not the average is responsible for inception (Refs. 12, 24). The near-wall region velocity field and the velocity fluctuations, u', are shown in Fig. 2 to give indication of the fluid velocity fluctuations the particles will be exposed to. The fluctuations are approximately 10%–20% of the local mean, and both the flow speed and turbulent intensity have a maximum at $r/D_{\text{disk}} \simeq 1$. This is probably an underestimate as the rotor tip vortices are not explicitly resolved.

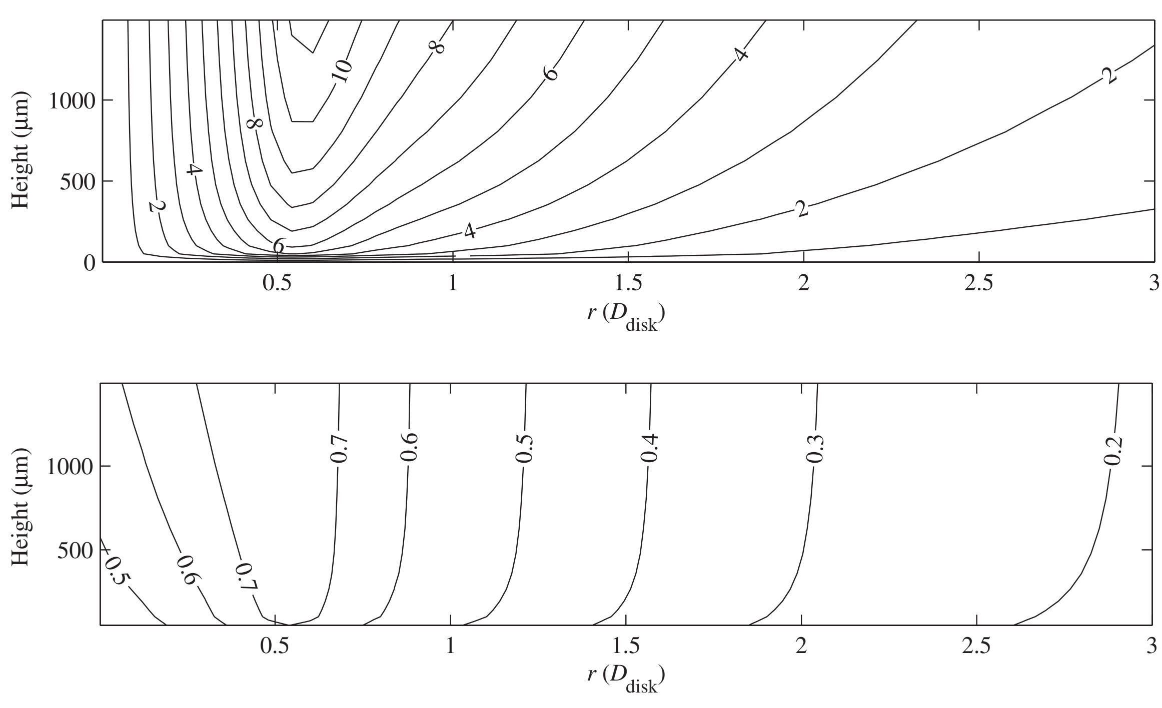

Fig. 2. Near-wall, $y < 1500\ \mu$m, fluid velocity magnitude field (ms^{-1}), and the RMS turbulent fluctuations (ms^{-1}).

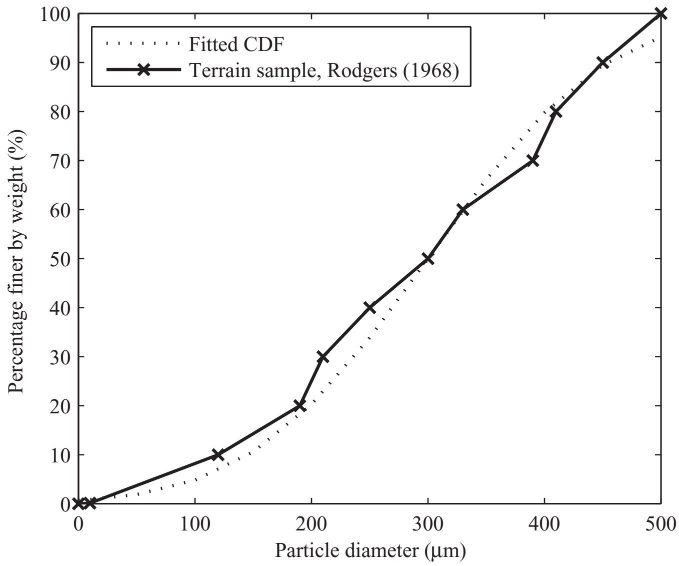

Fig. 3. Sand distributions from the study of Rodgers (Ref. 7).

Sand

Three sand grain sizes were chosen using a sand grain particle distribution function (PDF) generated from data collected by Rodgers (Ref. 7) of particles found on the desert floor, recreated here in Fig. 3. It was found that the sand diameter PDF closely followed a Gaussian distribution with mean 300 μm and standard deviation 120 μm. The distribution was calculated as a percentage by weight, and the maximum and minimum sieve size was 500 and 10 μm, respectively. For the following analysis, the force expressions for three particle sizes are evaluated: $D_p = 10$, 300, and 500 μm diameter, representing a small, medium, and large particles encountered on the surface of the desert, respectively. While the smaller particles contribute most to visual obscuration, the other sizes are investigated here for their role in the entrainment process via saltation.

A summary of the material properties of sand and air are given in Table 1. The values have been used in subsequent analysis.

Table 1. Physical properties of sand and air (20°C, 1 bar)[a]

Property	Sand (glass)	Air	Units
Density	2480	1.19	kg/m^3
Dynamic viscosity	N/A	1.82×10^{-5}	Ns/m^2
Surface energy	2×10^{-4}	N/A	N/m

[a]Refs. 47, 48.

Nondimensional Particle–Fluid Forces

The particle–fluid forces consist of two components from the traditional Basset–Boussinesq equation: drag and the Basset force and the transverse forces: Magnus and Saffman. The particle is also subject to gravity and, when in contact with other particles, friction and cohesion. The Basset force is related to the development of the boundary layer and the wake around the particle as a result of relative acceleration. The Magnus force gives lift due to relative rotation, and the Saffman force gives lift due to velocity gradient. The particle–fluid force expressions were nondimensionalized and compared for relative importance. Table 2 lists the nondimensional reference values and derivations. The velocity scale was chosen to be the disk velocity, and the length scales are the three particle diameters; the remaining scales are material properties or derivatives.

The nondimensionalized equation of motion is expressed in terms of reference forces and nondimensional forces in Eq. (4):

$$\frac{du_i^*}{dt^*} = [F_{D0}F_{D,i}^* + F_{B0}F_{B,i}^* + F_{M0}F_{M,i}^* + F_{L0}F_{L,i}^* + F_{G0}F_{G,i}^* + F_{P0}F_{P,i}^* + F_{Fr0}F_{Fr,i}^*] \tag{4}$$

where the forces are $F_D =$ drag, $F_B =$ Basset, $F_M =$ Magnus, $F_L =$ Saffman, $F_G =$ gravity, $F_P =$ cohesion, and $F_{Fr} =$ friction, $F_{\phi 0}$ has units of N/kg. The nondimensionalized force expressions are given in Table 3. Twice the turbulent velocity fluctuation from the $k-\epsilon$ turbulence model, $2u'$, was added to the mean flow field to give a peak velocity field (Ref. 30) and is used in all the force calculations. Cohesion was calculated between particles in a bed of equal size. Friction is calculated as the product of the friction coefficient and the normal reaction component.

In addition to the forces in Table 3, there is the lift experienced by a particle at rest on a wall in a flow. Following Mollinger and Nieuwstadt (Ref. 31), the nondimensional lift force is expressed in Eq. (5):

$$F_L^+ = p(a^+)^q \tag{5}$$

where $F_L^+ = \tilde{F}_L/\rho\nu^2$ and the nondimensional radius, a^+, is $a^+ = D_p u_\tau/2\nu$, where u_τ is the shear velocity and Re_τ the shear Reynolds number, $Re_\tau = D_p u_\tau/\nu$. In recent work by Zeng et al. in Ref. 32 and Rabinovich and Kalman in Ref. 33, values for p and q were collected for different limits of Re_τ. Saffman (Ref. 34) and Leighton and Acrivos in Ref. 35 provide values of $p = 6.46$, $q = 3$, and $p = 9.22$, $q = 4$, respectively, for $Re_\tau \ll 1$. For the range $0.6 < Re_\tau < 4$, experiments by Mollinger et al. (Ref. 31) give $p = 56.9$, $q = 1.87$. Hall extends the range, $Re_\tau > 6$, in Ref. 36 with values of $p = 20.9$, $q = 2.31$. For this flow field and the typical sand distribution $0 < Re_\tau < 40$, therefore, three expressionsneed to be used. For the low values of Re_τ, the chosen

Table 2. Reference parameters

Scale	Description	Symbol	Nondimensional	Value		
Length scale	Particle diameter	D_0	$D_0^* = x/D_0$	10 μm	300 μm	500 μm
Velocity scale	Bulk rotor flow speed	u_0	$u^* = u_i/u_0$	6.0 m/s	–	–
Fluid density scale	Air density	ρ_{f0}	$\rho_f^* = \rho_f/\rho_{f0}$	1.19 kg/m^3	–	–
Particle density scale	Sand density	ρ_{p0}	$\rho_p^* = \rho_p/\rho_{p0}$	2480 kg/m^3	–	–
Viscosity scale	Viscosity of air	μ_0	$\mu^* = \mu/\mu_0$	1.82×10^{-5} kg/ms	–	–
Timescale	Derived	D_0/u_0	$t^* = t(u_0/D_0)$	1.56×10^{-6}s	46.9×10^{-6}	78.1×10^{-6}
Surface energy scale	Surface energy of glass	σ_0	$\sigma^* = \sigma/\sigma_0$	2×10^{-4} Jm^{-2}	–	–
Gravity scale	Magnitude of gravity	g_0	$g = g_0 g^*$	9.81 m/s^2	–	–
Density ratio	Fluid to solid density	ρ_{f_0}/ρ_{p_0}	ρ_{f_0}/ρ_{p_0}	5.57×10^{-4}	–	–

Table 3. Forces and nondimensionalization

Force		F_ϕ	C_ϕ or f_ϕ	Refs.
Drag	F_{D0}	$\left[18 f_D \frac{\rho_{f0}}{\rho_{p0}} \frac{1}{Re_0}\right]$	$f_D = \begin{cases} 1 & Re_p \ll 1 \\ 1 + 0.15 {Re_p}^{0.687} & Re_p < 800 \end{cases}$	49, 50, 51
	F_D^*	$\left[\frac{\mu_f^*}{\rho_p^* D_p^{*2}} (u_i^* - v_i^*)\right]$		
Basset	F_{B0}	$\left[\frac{9C_B}{\sqrt{\pi}} \left(\frac{\rho_{f0}}{\rho_{p0}} \frac{1}{Re_0}\right)^{\frac{1}{2}}\right]$	$C_B = 2.88 + \frac{3.12}{(0.12 + A_c)^3}$ $A_c = \frac{\lvert u_{rel}\rvert^2}{2 r_p \frac{d\lvert u_i - v_i\rvert}{dt}}$	49, 52
	F_B^*	$\left[\left(\frac{1}{Re^* t^*}\right)^{\frac{1}{2}} \left(\int_0^t \frac{1}{\sqrt{(t^* - \tau^*)}} \frac{\mathrm{d}(u_i^* - v_i^*)}{\mathrm{d}\tau^*} \mathrm{d}\tau^* + \frac{(u_i^* - v_i^*)_0}{\sqrt{t^*}}\right)\right]$		
Magnus	F_{M0}	$\left[\frac{3}{4} C_M \frac{\rho_{f0}}{\rho_{p0}}\right]$	$C_{L,M} = 0.45 + \left(\frac{Re_{rot}}{Re_p} - 0.45\right) \exp\left(-0.05684 Re_{rot}^{0.4} Re_p^{0.3}\right)$	49, 53, 19
	F_M^*	$[e_{ijk} \Omega_j^* (u_k^* - v_k^*)]$	$Re_{rot} < 140$	
Saffman	F_{S0}	$\left[3.07 f_S \frac{\mu_0}{(u_0^2 \rho_{p0})} (Re_0)^{\frac{1}{2}}\right]$	$C_{L,S} = \begin{cases} (1 - 0.3314\sqrt{\beta_L}) \exp\left(-\frac{Re_p}{10}\right) + 0.3314\sqrt{\beta_L} & Re_p \leq 40 \\ 0.0524\sqrt{\beta_L Re_p} & Re_p > 40 \end{cases}$	49, 46
	F_S^*	$\left[\left(\frac{\mu^*}{D^{*2} \rho_p^*}\right)^{\frac{1}{2}} \left(\frac{e_{ijk}(u_j^* - v_j^*)\omega_{f,k}^*}{\lvert\omega_{f,i}^*\rvert^{\frac{1}{2}}}\right)\right]$	$\beta_L = Re_p \frac{\lvert\omega_{rel}\rvert}{\lvert u_{rel}\rvert}, \quad 0.005 < \beta_L < 0.4$	
Gravity	F_{G0}	$\left[\frac{1}{Fr_0^2}\right]$		
	F_G^*	g_i^*		
Cohesion	F_{P0}	$\left[6 f_p \frac{\sigma_0}{D_0 u_0 \rho_{p0}}\right]$	$f_p = \begin{cases} 1.5 & \text{JKR} \\ 2 & \text{DMT} \end{cases}$	54, 55, 38, 56
	F_P^*	$\left[\frac{\sigma^*}{D^{*2} \rho_p^*} r_i^*\right]$		
Friction	$F_{fr0} F_{fr}^*$	$C_{Fr}(F_{P0} F_{p,i}^* + F_{g0} F_{g,i}^* - F_{S0} F_{S,i}^* - F_{M0} F_{M,i}^*)$		

expression used is from Leighton and Acrivos as this fits experimental data of Ref. 31 better in the range $Re_\tau < 0.6$.

Nondimensional particle force analysis

The reference values from Tables 2 and 4 were applied to the expressions in Table 3 to find the relative importance of the forces for the typical scenario. The nondimensional variables, F_ϕ^*, are typically of order 0. The reference terms, $F_{\phi 0}$, have been evaluated and are given in Table 5 with the direction of action of the force. These results present only a general overview due to the highly inhomogeneous flow, demonstrated by the range of u seen in Fig. 2. However, the nondimensional procedure shows which forces dominate and which forces are completely negligible.

In the nondimensional analysis, the drag force is most significant for smaller particles and reasonably insignificant for the larger particles. The Basset force appears to be significant across all particle ranges. Magnus force has some presence for all particle ranges, as it is a transverse force it is competing with gravity and pull-off forces, for small particles pull-off is larger but for the large particles Magnus is comparable. The Saffman force is always very small and can be considered negligible as $F_M^* \gg F_S^*$. The particle weight is a significant force throughout; the pull-off force is stronger than gravity for the smallest particles, but reduces to similar order for the largest particles. The strength of the Basset force and the lower value of drag support the notion that the peak fluctuations cause inception (Ref. 21). Among the vertical forces, the retarding forces are strongest for the smallest particles but the Magnus lift force is sufficient to allow larger particles to entrain more readily, and this supports the concept of the initial entrainment of larger particles evidenced in Ref. 37. Because friction is proportional to the normal force, for the smaller particles the lift is small but with increased particle size the lift exceeds the cohesive and gravitational forces as indicated by negative friction, the values are still very small therefore fluctuations will be important.

Table 4. Nondimensional numbers

	Expression	Nondimensional	Value		
Particle diameter			10 μm	300 μm	500 μm
Reynolds number	$\rho_{f0} D_0 u_0 / \mu_{f0}$	Re_0	4.31	1.29×10^2	2.15×10^2
Froude number	$\sqrt{u_0^2 / g_0 D_0}$	Fr_0	646	118	91.4

Table 5. Force reference values for three particle sizes

Force reference	Direction	Particle Diameter, D_p (μm) 10	300	500
F_{D0}	→	$2.20 \times 10^{-3} f_D^*$	$7.34 \times 10^{-5} f_D^*$	$4.40 \times 10^{-5} f_D^*$
F_{B0}	→	$5.62 \times 10^{-2} C_B^*$	$1.03 \times 10^{-2} C_B^*$	$7.94 \times 10^{-3} C_B^*$
F_{M0}	↑	$3.60 \times 10^{-4} C_M^*$	$3.60 \times 10^{-4} C_M^*$	$3.60 \times 10^{-4} C_M^*$
F_{S0}	↑	$1.24 \times 10^{-9} f_S^*$	$6.79 \times 10^{-9} f_S^*$	$8.77 \times 10^{-9} f_S^*$
F_{G0}	↓	2.73×10^{-6}	8.18×10^{-5}	1.36×10^{-4}
F_{P0}	↓	$8.06 \times^{-3} f_P^*$	$2.69 \times 10^{-4} f_P^*$	$1.61 \times 10^{-4} f_P^*$
F_{Fr0}	←	$7.71 \times 10^{-3} C_{Fr}^*$	$-9.31 \times 10^{-6} C_{Fr}^*$	$-6.23 \times 10^{-5} C_{Fr}^*$

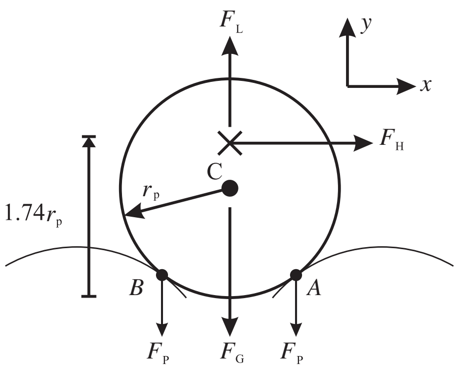

Fig. 4. Forces acting on a particle at rest on two particles.

Analysis of nondimensional forces for inception about an asperity

Inception occurs when the fluid forces acting on the particle are sufficient to exceed the resistive forces of gravity and cohesion. A sand particle on a bed of sand can be modeled as a sphere resting on two or more asperities, which are themselves spheres, as in Fig. 4. This approach, adopted by Ibrahim et al. (Ref. 37) and Ziskind et al. (Ref. 38), uses the moments to liberate the particle. Ziskind et al. include a full analysis of particle detachment from a flat plate as well as rocking about an asperity; here only the latter will be considered as the dusty ground is composed of particles upon particles not smooth surfaces. The analysis is as follows: Moments are calculated about the downwind asperity, A, the horizontal fluid force, F_H, acts at distance $0.74r_p$ above the center of the particle as suggested by Ibrahim et al. due to the shear du/dy. The lift and weight act at the center, cohesion acts at the contacts. The distance between asperities A and B is a. Resolving the moments about asperity A gives Eq. (6):

$$F_H r_p \left(0.74 + \left(r_p^2 - \frac{a^2}{4}\right)^{\frac{1}{2}}\right) - aF_P - (F_g - F_L) r_p \frac{a}{2} = 0 \quad (6)$$

such that the horizontal streamwise force required for motion becomes Eq. (7):

$$F_{H_{\text{crit}}} = \frac{aF_P + (F_g - F_L)\frac{r_p a}{2}}{r_p\left(0.74 + \left(r_p^2 - \frac{a^2}{4}\right)^{\frac{1}{2}}\right)} \quad (7)$$

Once the particle is freed from this stable position, it is still reliant on the lift forces to overcome gravity. As particles tend to occupy stable positions, it is the motion of larger particles, more exposed to the flow and with smaller asperity bases, that precede the suspension of the finer colloidal particles.

Nondimensionalizing Eq. (7) results in Eq. (8):

$$F_{H_{\text{crit}}} = \frac{F_{p0} a^* F_P^* + a^* D^* \left(F_{g0} \frac{D_0}{4} F_g^* - F_{S0} \frac{D_0}{4} F_S^* - F_{M0} \frac{D_0}{4} F_M^*\right)}{\frac{0.74}{2} D^* + \frac{D_0}{4} D^* (D^{*2} - a^{*2})^{\frac{1}{2}}} \quad (8)$$

Substituting values from Table 5 into Eq. (8) and ignoring the insignificant terms, $F_{g0} D_0$, $F_{S0} D_0$, and $F_{M0} D_0$, gives Eq. (9):

$$F_{H_{\text{crit}}} = \left[A_H \frac{a^* F_P^*}{D^*}\right] \quad (9)$$

where $A_{H,D=10} = 2.18 \times 10^{-2}$, $A_{H,D=300} = 7.27 \times 10^{-4}$, and $A_{H,D=500} = 4.36 \times 10^{-4}$.

F_H is the sum of all the fluid forces acting in the direction of the flow; the common force in this case is drag, but as seen in the previous analysis the Basset force is also potentially significant. Substituting the nondimensionalized drag force and the reference term from Table 5 gives Eq. (10):

$$F_{D_{\text{crit}}}^* = \left[9.90 \frac{a^*}{f_D D^*} F_P^*\right]_{10\ \mu\text{m}} = \left[9.90 \frac{a^*}{f_D D^*} F_P^*\right]_{300\ \mu\text{m}} = \left[9.90 \frac{a^*}{f_D D^*} F_P^*\right]_{500\ \mu\text{m}} \quad (10)$$

From this analysis, it is clear that the moment required by the drag force scales with the pull-off force. For the drag force to be capable of rocking the particle, there will need to be fluctuations to increase drag and a relatively small asperity base. Larger particles are more likely to be resting on smaller particles, will have a smaller a^*/D^* and will be easier to rock.

Repeating the above substitution for the Basset force yields Eq. (11):

$$F_{B_{\text{crit},i}}^* = \left[A_B \frac{a^*}{C_B D^*} F_P^*\right] \quad (11)$$

where $A_{B,D=10} = 0.388$, $A_{B,D=300} = 7.09 \times 10^{-2} \times 10^{-4}$, and $A_{B,D=500} = 5.49 \times 10^{-2}$.

This indicates that the Basset force is much more capable of causing inception than the drag force; this indirectly supports the rock-n-roll model, described in Ref. 39, based on the premise that a particle will oscillate by pivoting backward and forward around one of the asperities. The analysis in both cases agrees with the notion of Ibrahim et al. that larger particles are suspended more readily than fine particles.

RANS Flow-Particle Analysis

In this section the RANS flow field is applied to the particles; first their location in the boundary layer is considered, and second the particle-fluid force expressions described earlier are applied to the near ground region of the flow field and results discussed.

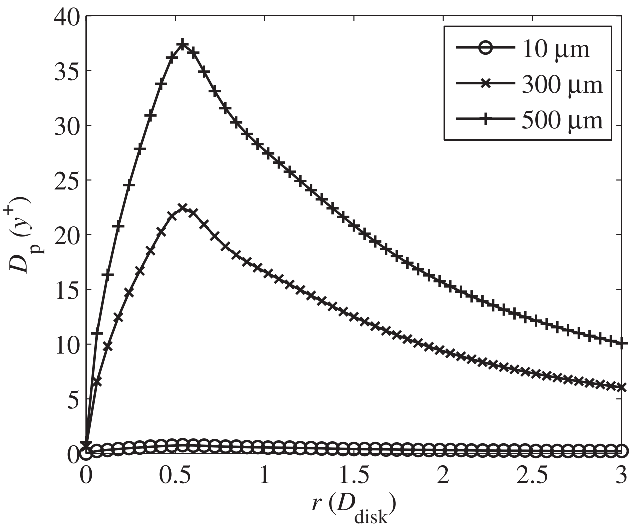

Fig. 5. D_P/y^+ for three particle diameters computed across the radial extent of the domain.

Boundary layer analysis

To see where the particles rest in the turbulent boundary layer, Fig. 5 shows D_p/y^+_{wall}, where y^+_{wall} is the nondimensional boundary layer height for radial positions on the wall. It can be seen that the smallest particles are well within the viscous sublayer and so are subject to the physics and lift forces given in Refs. 34 and 35, whereas the larger particles protrude into the buffer zone and are subject to the wall lift forces described in Refs. 31 and 36; for these particles, inertial effects are significant and the assumption of a linear shear layer (Ref. 40) is not entirely valid. The Philips and Brown model (Ref. 15) assumes a single threshold velocity without consideration of where the particle exists in the boundary layer, and the Wachspress model (Ref. 14) makes no allowances for the change of physics involved between particles in the viscous and those in the inertial layers.

The Stokes number is the ratio of particle relaxation time to fluid timescales; it is an indicator of the particles reaction to unsteady flow features such as turbulent eddies. The timescales of the larger eddies were found using turbulent kinetic energy and dissipation rate $\tau_f = \frac{k}{\epsilon}$. In this flow, $St_{10} > 1$ for $y^+/D_p < 1$ indicating that a particle on the surface will not resonate in response to turbulent eddies close to the wall. The larger particles also show that they are unlikely to be stimulated by the near-wall fluctuations as $St_{300} \gg 1$ and $St_{500} \gg 1$. It has been suggested in the literature, e.g., in Refs. 41 and 6, that the flow can cause particles to resonate in situ before being ejected. The resonance entrainment model (Ref. 6) assumes that energy from the turbulent fluctuations causes the particle to resonate within the adhesive potential well; the particle detaches from the surface when it has acquired enough energy to escape from the well. The evidence here suggests that the drag force is not capable of this concept as $St \gg 1$.

Particle forces

The particle forces were calculated for the three diameters of 10, 300, and 500 μm in the near-wall region $y < 3D_p$ and nondimensionalized by the sum of cohesion and gravity; $F_\phi/(F_g + F_p)$. In all cases, the particle is assumed stationary relative to the ground and not rotating. The value at a height of $y \simeq 0.5D_p$ is of particular interest as that is the location of the resting particles center of mass. For the regions where $y > D_p$, the particle is unlikely to be stationary so forces in this region are overestimated; however, it is useful to have an indication of the fluid forces a particle is likely to encounter should it leave the ground.

The drag forces (Fig. 6) are significant for all but the smallest particle sizes. The region $0.5 < r/D_{\text{disk}} < 1.5$ is of most significance, here the forces are strongest. The horizontal region where the drag is significant is very large, providing a large surface for potential inception. The trends here agree with those indicated by the nondimensional analysis; for the smallest particles, the drag is very large—but cohesion holds the particles back; for the medium and large particles, the drag is of similar order to the retarding forces.

The Basset force requires relative acceleration history over time. To simulate this from, the RANS results the larger eddy timescale, $\tau_f = k/\epsilon$ is used as the period and twice the root mean square (RMS) fluctuation, $2u'$, is used as the amplitude. The relative acceleration is $\dot{u} = u'\frac{2\pi}{\tau_f}\cos(t\frac{2\pi}{\tau_f})$, where t is time. These forces were all insignificant compared to the sum of cohesion and gravity for this flow field. However, the fluctuations in this flow will not be the same as those in flow with ground vortex interaction; this force should not be overlooked in an unsteady rotor analysis.

The wall-induced lift force is quantified in Fig. 7 for the three diameters. The peak is in the region of $r/D_{\text{disk}} \simeq 0.5$. The smaller particles are subject to strong lift forces but are dominated by the cohesive forces; the medium-sized particles are capable of being entrained by these flow conditions, but the largest particles are too heavy.

Summing the forces acting on the particle gives a resultant force vector, and these have been plotted for six radial particle locations in Fig. 8. A vector length of one radius indicates a resultant force equal in magnitude to $F_G + F_P$. It is clear that the medium particles are the most likely to be incepted, the region $0.25 < r/D_{\text{disk}} < 1.25$ showing the strongest resultant forces.

Effects of Blade Tip Vortices

It is clear from the literature noted above that the tip vortices present in the rotor wake seem to be a significant factor in the entrainment process. In this section, we follow the approach of Ananthan et al. (Ref. 42) to estimate the initial location and strength of tip vortices produced by the rotor IGE and the transport of these vortices toward and across the ground plane.

The wake boundary is found by following a streamline from the rotor tip, the tip vortices are known to travel along this streamline (Ref. 10). As the tip vortices convect downward, two processes act upon them: diffusion and strain. Diffusion acts to increase the radius of the vortex core, whereas positive strain, stretching the vortex filament, decreases the vortex core radius and conservation of circulation causes the filament to spin up. As in the Ananthan et al. study, the radius of the vortex is defined as the radial distance from zero to the peak swirl velocity. A third process also occurs due to the influence of other nearby vortices; the induced velocity of one vortex will influence the position of those around it and vice versa, resulting in filaments twisting around each other and even joining up (Ref. 11). For a near ground vortex, the induced velocity would lower the pressure between the vortex and the ground and suck the vortex downward. The first two of these processes are considered in this analysis.

The tip vortices of a helicopter are helical; for the purposes of calculation, they are considered to be discrete rings in this axisymmetric simulation. The vortices follow the wake boundary; therefore, the strain at any time can be given as the relative change in the circumference of the vortex ring, that is $\epsilon(\zeta) = \frac{r_v(\zeta) - r_{v0}}{r_{v0}}$, where $r_v(\zeta)$ is the radius of the vortex ring at wake age $\zeta = \Omega t$ and r_{v0} is the radius of the rotor blade. The vortex core radius, r_c, following a given strain can be found using

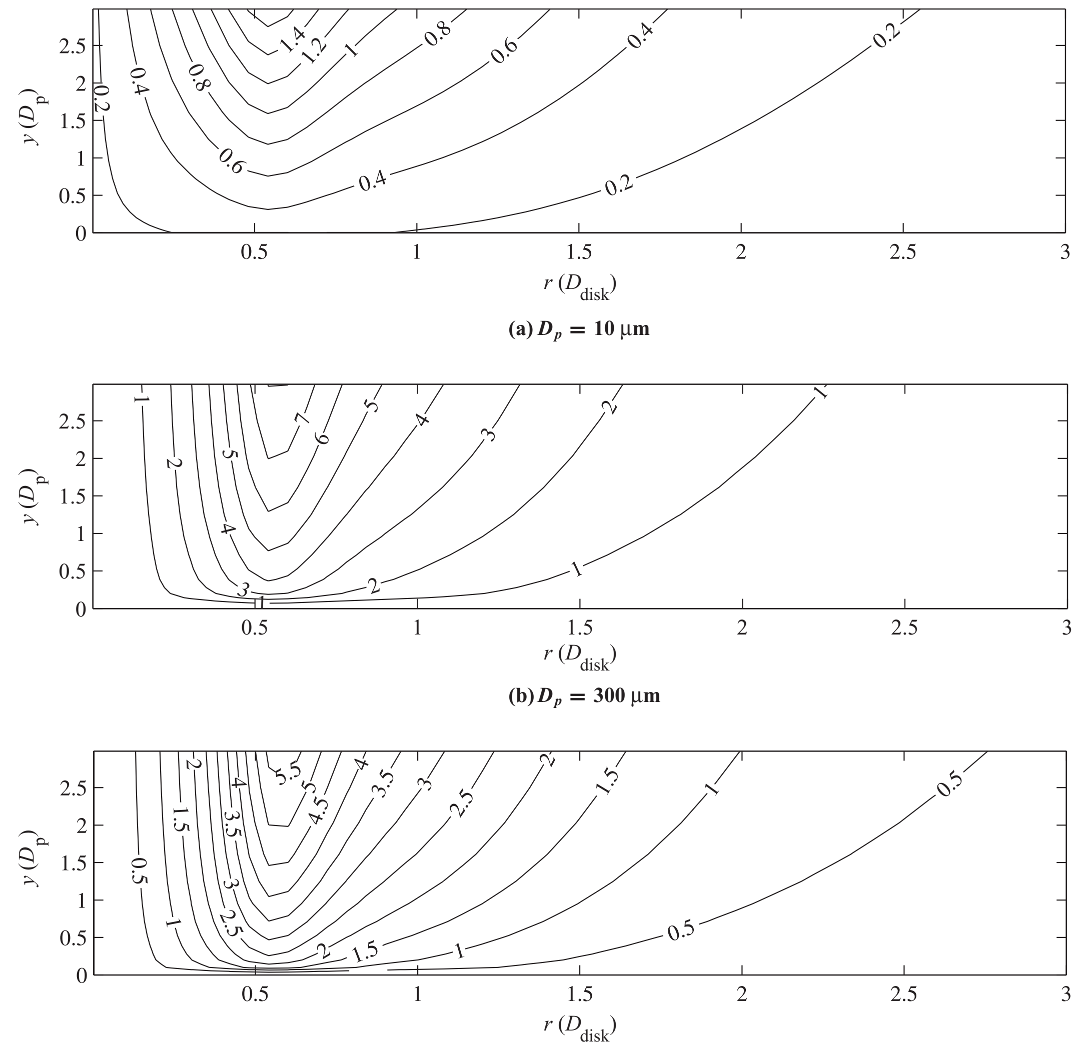

(a) $D_p = 10$ μm

(b) $D_p = 300$ μm

(c) $D_p = 500$ μm

Fig. 6. Drag force field for three particle sizes, nondimensionalized by weight and cohesion. Plot of the near ground region, $y < 3D_p$, and radially from hub to $3D_{disk}$.

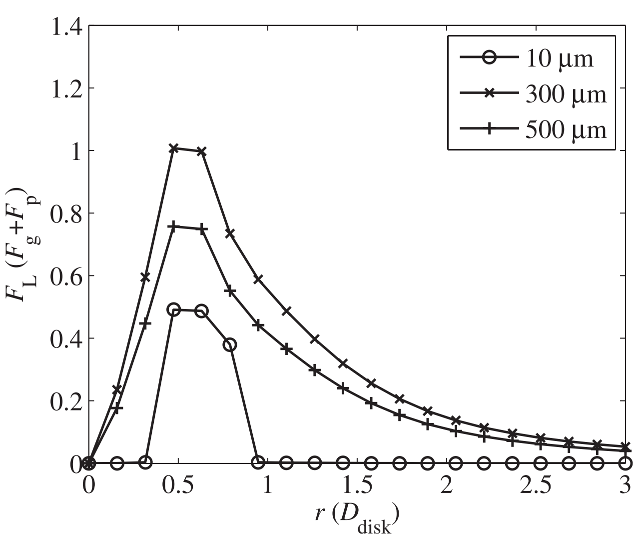

Fig. 7. Induced lift force for wall bound particles. Three diameters are plotted.

Eq. (12) from Ref. 42:

$$r_c(\zeta) = r_{c0}\frac{1}{\sqrt{1+\epsilon(\zeta)}} \tag{12}$$

where r_{c0} is the vortex core radius at $\zeta = 0$. Diffusion acts to increase the vortex radius as described by Lamb and Oseen (Ref. 43) and modified by Squires (Ref. 44), defined by Eq. (13):

$$r_c(\zeta) = \sqrt{r_{c0}^2 + \frac{4\alpha\delta\nu\zeta}{\Omega}} \tag{13}$$

where α is a constant found to be 1.25643 (Ref. 43), δ is an eddy viscosity parameter $\delta = 1 + a_1(\Gamma_v/\nu)$ with $a_1 = 2 \times 10^{-4}$ from the Ananthan et al. study, and Γ_v is the tip vortex circulation. The tip vortex circulation can be estimated from the lift, given two blades then $\Gamma_v = L/(R^2\Omega\rho)$, where Ω is the blade angular velocity. Combining the effects of diffusion, Eq. (13), and filament strain, Eq. (12), gives Eq. (14):

$$r_c(\zeta) = \sqrt{r_{c0}^2 + \frac{4\alpha\delta\nu\zeta}{\Omega}}\frac{1}{\sqrt{1+\epsilon(\zeta)}} \tag{14}$$

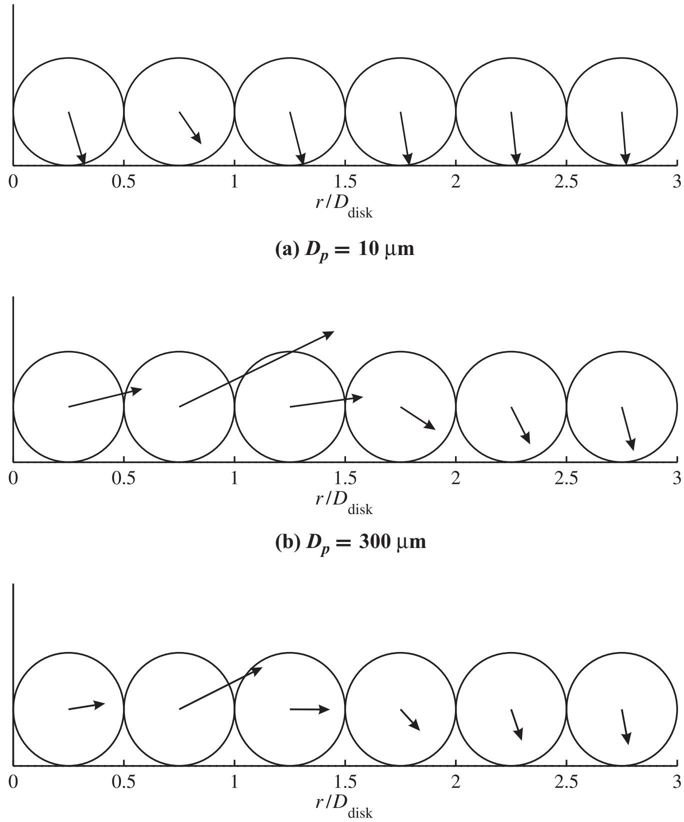

(a) $D_p = 10$ μm

(b) $D_p = 300$ μm

(c) $D_p = 500$ μm

Fig. 8. Resultant force vectors for wall-bounded particles at varying radial positions. Arrow length of 1 radius indicates $F_{\mathrm{Total}} = F_G + F_P$.

Using the previously defined lift value, $L = 8800$ kN, using a typical blade rotational speed of $\Omega = 340$ rpm $= 35.6$ rads^{-1} and estimating the initial vortex core radius using the PIV results of Johnson to be $r_{c0} = 0.03R$, we can quantify the vortex initialization. The inset in Fig. 9 compares the size of the vortex radius over time using the diffusion model with the combined diffusion-strain model. In the combined model, r_c is larger where negative strain caused by the contraction of the rotor wake is present and similarly when strain is positive as the wake expands across the ground r_c decreases more rapidly than the expanding process of diffusion.

Having found r_c the swirl velocity around the vortex can be described using the Lamb–Oseen model (Ref. 43) in Eq. (15):

$$V_\theta(\bar{r}) = \frac{\Gamma_v}{2\pi r_c} \frac{1 - e^{-\alpha \bar{r}^2}}{\bar{r}} \tag{15}$$

where $\bar{r} = r_v/r_c$ is the relative radial distance from the vortex core and r_v is the radial distance from the vortex core.

Figure 9 indicates the swirl velocity profile for a series of vortex positions; these are reasonable when compared with the predictions of Ananthan et al. in Ref. 42 and Ramasamy and Leishman in Ref. 45 and compare qualitatively with the smoke visualizations of Lee et al. in Ref. 10. The swirl velocity seen at the ground has a value of $V_{\theta,\mathrm{ground}} \simeq 1\mathrm{ms}^{-1}$ and is fairly invariant to radial position in contrast with the average flow field. The fluctuations reported by the RANS results were of the order of 10%–20% of the mean flow with the peak beneath the rotor tip. The vortices, however, represent higher fluctuations as much as 100% of the mean flow for the near ground distances presented in Fig. 2.

The vortex is a highly two-dimensional flow feature; as the vortex passes a fixed point on the ground, the vortex swirl velocity is first an upwash, then a horizontal flow as the vortex is directly above and finally when the vortex has passed the flow is directed toward the ground. The velocity magnitude peaks when the vortex is directly overhead. The increase in horizontal flow velocity and velocity gradient from the passing vortex will increase the range of particle sizes stimulated and increase the spatial entrainment region. The vortices also provide the vertical flow that pulls particles up and away from the ground.

Discussion

The aim of the analysis is to discover which forces are capable of causing or contributing to particle inception within the downwash of a full-scale helicopter flow. The nondimensional analysis gave some indication as to the influence of the different forces acting on the particle, but the influence of the nondimensional term, the deviation from reference values, was not quantified. There are some differences between the behavior indicated by the nondimensional analysis and the forces from the RANS model; this is due to the highly inhomogeneous flow. The results prove that the flow field cannot be characterized with a single set of scales, and similarly the RANS results show that the entrainment cannot be characterized by one set of scales either given that each particle size behaves differently.

The RANS results indicate that of the fluid forces presented only drag and wall-induced lift contribute significantly. Looking at Fig. 8, the drag force would easily be sufficient to induce movement through rocking about an asperity as proposed by Ziskind et al. in Ref. 38. There is experimental evidence that the larger particles are the first to be incepted in parallel flows (Ref. 46), correlating here in Fig. 8, emphasizing the varying significance of the cohesion force across particle sizes as the key factor.

Given that the boundary layer is spatially developing and a range of particle sizes exist, no one force is dominant but the lift–drag combination is the driving inception force. For a Lagrangian entrainment model, the cohesion, drag, and wall-induced lift are critical for understanding the location and size of the incipient particles. In this flow field, the incipient motion is of the middle-sized particles in the region $0.25 < r < 1.5$, although the vortices may be able to expand that as the horizontal velocity they induce near the ground does not decay as rapidly as the mean flow. The lift and drag both peak in this region, and the force is enough for direct lift off or to initiate motion along the surface. The larger particles would rush along the surface knocking smaller particles breaking the cohesive forces enough that they can be entrained. These particles would continue in the wall jet until they met an upwash; the smaller particles would be taken up, but the larger particles would not be as influenced. The larger particles would continue to saltate along the ground and cause subsequent fine particle entrainment. If these particles meet an upwash, they will be carried upward as well. A pattern of particle entrainment peaking around radially expanding vortices is visible in photographs of brownout and experimental observations of Lee et al. (Ref. 10) and Johnson et al. (Ref. 11).

The analytical tip vortex assessment looks at what is essentially a large-scale inviscid feature; the turbulent fluctuations discussed in mean flow field results are a result of the near-wall boundary layer, a viscous flow feature with much smaller scales. Both the near-wall boundary layer and the tip vortices are present in the real-world rotor wake; the vortices provide an increase in horizontal velocity near the wall and upwash in the near-wall region, and the boundary layer is where all the particles lie before inception. The location of the particle in the boundary layer is shown by the RANS results to affect the aerodynamic

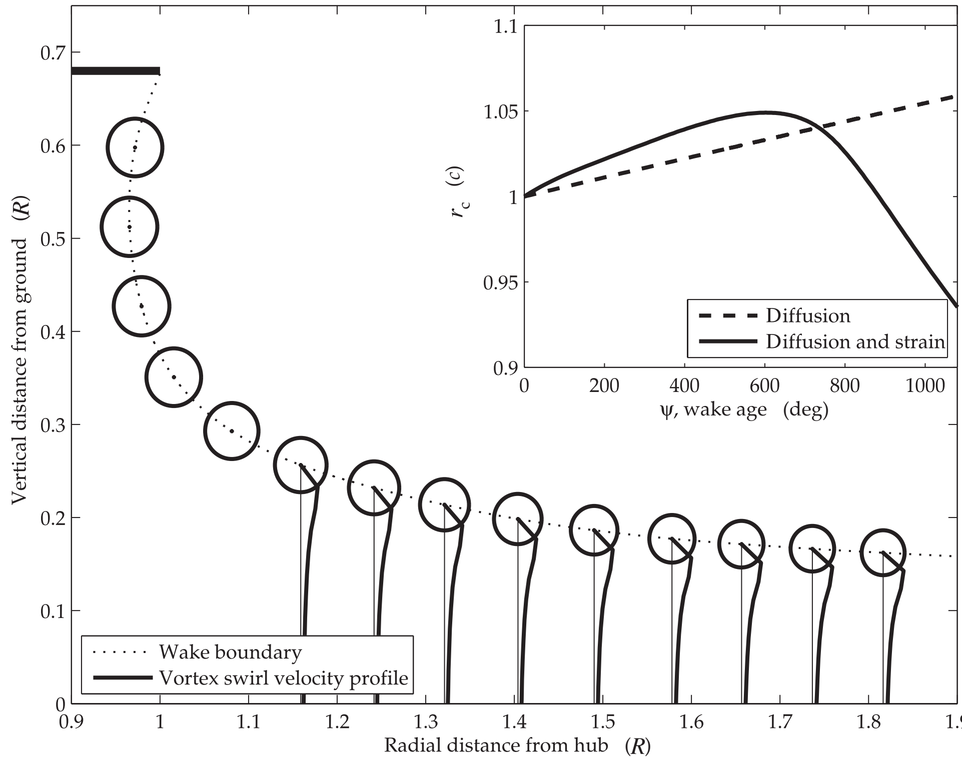

Fig. 9. Vortex core progression in the axisymmetric flow field. Inset figure compares vortex core growth with and without strain effects.

forces on the particle; the passing vortex will alter the boundary layer structure. Combining the results of the RANS analysis with the analytical tip vortex assessment leads us to believe that the interaction of these two processes, inviscid large-scale tip vortices and viscous small-scale fluctuating boundary layer structures, is the key to the deterministic Lagrangian entrainment model.

Of the entrainment models reviewed, it is difficult to say which best corroborate. The wall-induced lift force is based on the friction velocity as are the aeolian mass flux models; this will give them similar behavior if the aeolian parameters are tuned appropriately. Only the small particles are accounted for in the particle-tracking models, assuming that saltation is confined to a near ground region is appropriate as the wall-induced lift diminishes as the particle moves away from the wall so larger particles will not lift very high. However, the flow is highly inhomogeneous and the size of particles that can be entrained will change with radial position; this will subsequently change the saltation characteristics as well. A higher order unsteady analysis is required to study the evolution of the particle forces spatially and temporally and to determine how they contribute to entrainment as a whole.

Concluding Remarks

The aim was to discover which particle forces are crucial to a physics-based Lagrangian entrainment model for use with rotorcraft simulations. Presented here is a scaling analysis for the common fluid–particle forces with typical particle sizes using nondimensional analysis and time-averaged flow field velocities. The nondimensional analysis indicated that the Saffman force could be ignored. Comparing the RANS results with the nondimensional analysis demonstrated that the flow is highly inhomogeneous and that using nondimensional analysis to find relative importance was difficult to interpret. The flow field showed that the smallest particles, and those primarily responsible for the visual obscuration, sit within the viscous boundary layer whereas large particles are well outside it. This analysis has reinforced the notion that larger particles are excited before small particles; it has highlighted the importance of wall-bounded lift, but dismissed the shear-based Saffman lift. Cohesion controls the particle dynamics at the smallest scale, and weight controls them at the largest scale; the medium-sized particles are the ones of most interest as these are the ones that will be first stimulated into motion, and it is speculated that these will drive saltation. The analytical tip vortex assessment revealed that the vortices will likely increase the entrainment area through the increase in horizontal flow speed. The vortices will alter the structure of the boundary layer and in doing so change the aerodynamic forces on the particles, and these vortices also provide the vital upwash that blows the liberated particles upward into the large clouds that cause brownout.

The complexity of the problem is not easily captured, and the complex arrangement of the particle bed, the powerful vortex–ground interaction, and the particle saltation are all potentially significant factors. The union of the inviscid tip vortices and the viscous boundary layer development on the ground is the solution to this problem.

References

[1]Colby, S., "Military Spin," *Aviation Today–Rotor & Wing*, Vol. 39, March 2005.

[2]Sabbagh, L., "Flying Blind in Iraq: U.S. Helicopters Navigate Real Desert Storms," *Popular Mechanics*, Vol. 3, October 2006.

[3]Krantz, R., "Concern Network," *Air Medical Journal*, Vol. 21, (6), 2002, p. 6.

[4]Cao, Z., "Turbulent Bursting-Based Sediment Entrainment Function," *Journal of Hydraulic Engineering*, Vol. 123, (3), 1997, pp. 233–236.

[5]Guingo, M., and Minier, J.-P., "A New Model for the Simulation of Particle Resuspension by Turbulent Flows Based on a Stochastic Description of Wall Roughness and Adhesion Forces," *Journal of Aerosol Science*, Vol. 39, (11), 2008, pp. 957–973.

[6]Reeks, M. W., Reed, J., and Hall, D., "On the Resuspension of Small Particles by a Turbulent Flow," *Journal of Physics D: Applied Physics*, Vol. 21, (4), 1988, p. 574.

[7]Rodgers, S. J., "Evaluation of the Dust Cloud Generated by Helicopter Rotor Downwash," USAAVLABS Technical Report 67-81, March 1968.

[8]Gillies, J., Etyemezian, V., Kuhns, H., McAlpine, J., King, J., Uppapalli, S., Nikolich, G., and Engelbrecht, J., "Dust Emissions Created by Low-Level Rotary-Winged Aircraft Flight over Desert Surfaces," *Atmospheric Environment*, Vol. 44, (8), 2010, pp. 1043–1053.

[9]Cowherd, C., Jr., "Sandblaster 2 Support of See-Through Technologies for Particulate Brownout- Task 5 Final Technical Report," Midwest Research Institute, MRI Project No. 110565 under DARPA Contract No. W31P4Q-07-C-0215, October 31, 2007.

[10]Lee, T. E., Leishman, J. G., and Ramasamy, M., "Fluid Dynamics of Interacting Blade Tip Vortices with a Ground Plane," *Journal of the American Helicopter Society*, **55**, 022005 (2010).

[11]Johnson, B., Leishman, J. G., and Sydney, A., "Investigation of Sediment Entrainment Using Dual-Phase, High-Speed Particle Image Velocimetry," *Journal of the American Helicopter Society*, **55**, 042003 (2010).

[12]Haehnel, R., and Dade, W., "Physics of Particle Entrainment under the Influence of an Impinging Jet," Proceedings of Army Science Conference, Orlando, FL, December 1–4, 2008.

[13]McAlpine, J., Koracin, D., Boyle, D., Gillies, J., and McDonald, E., "Development of a Rotorcraft Dust-Emission Parameterization Using a CFD Model," *Environmental Fluid Mechanics*, Vol. 10, 2010, pp. 691–710.

[14]Wachspress, D. A., Whitehouse, G. R., Keller, J. D., Yu, K., Gilmore, P., Dorsett, M., and McClure, K., "A High-Fidelity Brownout Model for Real-Time Flight Simulations and Trainers," American Helicopter Society 65th Annual Forum Proceedings, Grapevine, TX, May 27–29, 2009.

[15]Philips, C., and Brown, R. E., "Eulerian Simulation of the Fluid Dynamics of Helicopter Brownout," American Helicopter Society 64th Annual Forum Proceedings, Montreal, Canada, April 29–May 1, 2008.

[16]D'Andrea, A., and Scorcelletti, F., "Enhanced Numerical Simulations of Helicopter Landing Maneuvers in Brownout Conditions," American Helicopter Society 66th Annual Forum Proceedings, Phoenix, AZ, May 11–13, 2010.

[17]Syal, M., Govindarajan, B., and Leishman, J. G., "Mesoscale Sediment Tracking Methodology to Analyze Brownout Cloud Developments," American Helicopter Society 66th Annual Forum Proceedings, Phoenix, AZ, May 11–13, 2010.

[18]Lu, H., and Shao, Y., "Toward Quantitative Prediction of Dust Storms: An Integrated Wind Erosion Modelling System and Its Applications," *Environmental Modelling & Software*, Vol. 16, (3), 2001, pp. 233–249.

[19]White, B. R., "Soil Transport by Winds on Mars," *Journal of Geophysical Research*, Vol. 84, 1979, pp. 4643–4651.

[20]Bagnold, R. A., *The Physics of Blown Sand and Desert Dunes*, 2nd ed., Methuen, London, 1954.

[21]Bauer, B. O., Yi, J., Namikas, S. L., and Sherman, D. J., "Event Detection and Conditional Averaging in Unsteady Aeolian Systems," *Journal of Arid Environments*, Vol. 39, (3), 1998, pp. 345–375.

[22]Butterfield, G. R., "Transitional Behaviour of Saltation: Wind Tunnel Observations of Unsteady Winds," *Journal of Arid Environments*, Vol. 39, 1998, pp. 377–394.

[23]Spies, P.-J., and McEwan, I. K., "Equilibration of Saltation," *Earth Surface Processes and Landforms*, Vol. 25, (4), 2000, pp. 437–453.

[24]Sterk, G., Jacobs, A. F. G., and Boxel, J. H. V., "The Effect of Turbulent Flow Structures on Saltation Sand Transport in the Atmospheric Boundary Layer," *Earth Surface Processes and Landforms*, Vol. 23, 1998, pp. 877–887.

[25]Ardey, N., and Mayinger, F., "Aerosol Resuspension by Highly Transient Containment Flow: Insights by Means of Laser Optical Methods," *Kerntechnik*, Vol. 63, 1998, pp. 68–75.

[26]Marchioli, C., Armenio, V., Salvetti, M. V., and Soldati, A., "Mechanisms for Deposition and Resuspension of Heavy Particles in Turbulent Flow over Wavy Interfaces," *Physics of Fluids*, Vol. 18, (2), 2006, 025102.

[27]Shih, T.-H., Liou, W. W., Shabbir, A., Yang, Z., and Zhu, J., "A New *k*-epsilon Eddy Viscosity Model for High Reynolds Number Turbulent Flows," *Computers & Fluids*, Vol. 24, (3), 1995, pp. 227–238.

[28]Kim, S.-E., and Choudhury, D., "A Near-Wall Treatment Using Wall Functions Sensitized to Pressure Gradient," Proceedings of the ASME/JSME Fluids Engineering and Laser Anemometry Conference and Exhibition, Separated and Complex Flows, Hilton Head, SC, August 13–18, 1995, pp. 273–280.

[29]Conlisk, A. T., "Modern Helicopter Rotor Aerodynamics," *Progress in Aerospace Sciences*, Vol. 37, (5), 2001, pp. 419–476.

[30]Schlichting, H., Gersten, K., Krause, E., and Oertel, H., Jr., *Boundary-Layer Theory*, Springer, Berlin, Germany, 2000, English translation of the 9th German completely revised edition, Chap. 16.

[31]Mollinger, A. M., and Nieuwstadt, F. T. M., "Measurement of the Lift Force on a Particle Fixed to the Wall in the Viscous Sublayer of a Fully Developed Turbulent Boundary Layer," *Journal of Fluid Mechanics*, Vol. 316, 1996, pp. 285–306.

[32]Zeng, L., Najjar, F., Balachandar, S., and Fischer, P., "Forces on a Finite-Sized Particle Located Close to a Wall in a Linear Shear Flow," *Physics of Fluids*, Vol. 21, (3), 2009, 033302.

[33]Rabinovich, E., and Kalman, H., "Incipient Motion of Individual Particles in Horizontal Particle-Fluid Systems: An Experimental Analysis," *Powder Technology*, Vol. 192, (3), 2009, pp. 318–325.

[34]Saffman, P. G., "The Lift on a Small Sphere in a Slow Shear Flow," *Journal of Fluid Mechanics*, Vol. 22, (2), 1965, pp. 385–400.

[35]Leighton, D., and Acrivos, A., "Viscous Resuspension," *Chemical Engineering Science*, Vol. 41, (6), 1986, pp. 1377–1384.

[36]Hall, D., "Measurements of the Mean Force on a Particle near a Boundary in Turbulent Flow," *Journal of Fluid Mechanics*, Vol. 187, 1988, pp. 451–466.

[37]Ibrahim, A., Dunn, P., and Qazi, M., "Experiments and Validation of a Model for Microparticle Detachment from a Surface by Turbulent Air Flow," *Journal of Aerosol Science*, Vol. 39, (8), 2008, pp. 645–656.

[38]Ziskind, G., Fichman, M., and Gutfinger, C., "Adhesion Moment Model for Estimating Particle Detachment from a Surface," *Journal of Aerosol Science*, Vol. 28, (4), 1997, pp. 623–634.

[39]Reeks, M. W., and Hall, D., "Kinetic Models for Particle Resuspension in Turbulent Flows: Theory and Measurement," *Journal of Aerosol Science*, Vol. 32, (1), 2001, pp. 1–31.

[40]Pope, S. B., *Turbulent Flows*, Cambridge University Press, Cambridge, UK, 2000, Chap. 7.

[41]Vainshtein, P., Ziskind, G., Fichman, M., and C.Gutfinger, "Kinetic Model of Particle Resuspension by Drag Force," *Physical Review Letters*, Vol. 78, (3), 1997, pp. 551–554.

[42]Ananthan, S., and Leishman, J. G., "Role of Filament Strain in the Free-Vortex Modeling of Rotor Wakes," *Journal of the American Helicopter Society*, Vol. 49, (2), 2004, pp. 176–191.

[43]Lamb, S. H., *Hydrodynamics*, Cambridge University Press, Cambridge, UK, 1932, pp. 592–593, 668–669.

[44]Squires, H. B., "The Growth of a Vortex in a Turbulent Flow," *Aeronautical Quarterly*, Vol. 16, August 1965, pp. 302–306.

[45]Ramasamy, M., and Leishman, J. G., "The Interdependence of Straining and Viscous Diffusion Effects on Vorticity in Rotor Flow Fields," American Helicopter Society 59th Annual Forum Proceedings and Technology Display, Phoenix, AZ, May 6–8, 2003.

[46]Zou, X.-Y., Cheng, H., Zhang, C.-L., and Zhao, Y.-Z., "Effects of the Magnus and Saffman Forces on the Saltation Trajectories of Sand Grain," *Geomorphology*, Vol. 90, (1–2), 2007, pp. 11–22.

[47]Calvert, J. R., and Farrar, R. A., editors, *An Engineering Data Book*, Palgrave, Suffolk, UK, 1999, Chap. 7.2.

[48]Jones, R., Pollock, H. M., Geldart, D., and Verlinden, A., "Inter-Particle Forces in Cohesive Powders Studied by AFM: Effects of Relative Humidity, Particle Size and Wall Adhesion," *Powder Technology*, Vol. 132, (2–3), 2003, pp. 196–210.

[49]Michaelides, E., *Particles, Bubbles & Drops: Their Motion, Heat and Mass Transfer*, World Scientific, Singapore, 2006, Chap. 2.6.

[50]Schiller, L., and Neumann, A., "Uber die Grundlegenden Berechungen bei der Schwerkraftaufbereitung," *Vereines Deutscher Ingenieure*, Vol. 77, 1933, pp. 318–320.

[51]Bagchi, P., and Balachandar, S., "Effect of Free Rotation on the Motion of a Solid Sphere in Linear Shear Flow at Moderate Re," *Physics of Fluids*, Vol. 14, 2002, pp. 2719–2737.

[52]Odar, F., and Hamilton, W. S., "Forces on a Sphere Accelerating in a Viscous Fluid," *Journal of Fluid Mechanics*, Vol. 18, (2), 1964, pp. 302–314.

[53]Crowe, C. T., Roberson, J. A., and Elger, D. F., *Engineering Fluid Mechanics*, 7th ed., Wiley, Hoboken, NJ, 2001, p. 504.

[54]Derjaguin, B. V., Muller, V. M., and Toporov, Y. P., "Effect of Contact Deformations on the Adhesion of Particles," *Journal of Colloid and Interface Science*, Vol. 53, (2), 1975, pp. 314–326.

[55]Johnson, K. L., Kendall, K., and Roberts, A. D., "Surface Energy and the Contact of Elastic Solids," *Proceedings of the Royal Society*, Vol. A324, 1971, pp. 301–313.

[56]Maugis, D., "Adhesion of Spheres: The JKR-DMT Transition Using a Dugdale Model," *Journal of Colloid and Interface Science*, Vol. 150, (1), 1992, pp. 243–269.